



Probability of radial anisotropy in the deep mantle

K. Visser^{a,*}, J. Trampert^a, S. Lebedev^a, B.L.N. Kennett^b

^a Department of Earth Sciences, Utrecht University, Utrecht 3584 CD, The Netherlands

^b Research School of Earth Sciences, The Australian National University, Canberra, Australia

ARTICLE INFO

Article history:

Received 19 December 2007

Received in revised form 12 March 2008

Accepted 13 March 2008

Available online 9 April 2008

Editor: R.D. van der Hilst

Keywords:

radial anisotropy

higher modes

phase velocities

surface waves

ABSTRACT

It is well established that the Earth's uppermost mantle is anisotropic, but observations of anisotropy in the deeper mantle have been more ambiguous. Radial anisotropy, the discrepancy between Love and Rayleigh waves, was included in the top 220 km of PREM, but there is no consensus whether anisotropy is present below that depth. Fundamental mode surface waves, for commonly used periods up to 200 s, are sensitive to structure in the first few hundred kilometers and therefore do not provide information on anisotropy below. Higher mode surface waves, however, have sensitivities that extend to and below the transition zone and should thus give insight about anisotropy at greater depths, but they are very difficult to measure. We previously developed a new technique to measure higher mode surface wave phase velocities with consistent uncertainties. These data are used here to construct probability density functions of a radially anisotropic Earth model down to approximately 1500 km. In the uppermost mantle, we obtain a high probability of faster horizontally polarized shear wave speed, likely to be related to plate motion. In the asthenosphere and transition zone, however, we find a high probability of faster vertically polarized shear wave speed. To a depth of 1500 km in the lower mantle, we see no significant shear wave anisotropy. This is consistent with results from laboratory measurements which show that lower mantle minerals are anisotropic but LPO is unlikely to develop in the pressure–temperature conditions present in the mid-mantle.

© 2008 Elsevier B.V. All rights reserved.

1. Introduction

Radial and azimuthal anisotropy are different expressions of the underlying general anisotropy of the Earth's interior. The source of anisotropy in the mantle is usually assumed to be the alignment (lattice preferred orientation or LPO) of intrinsically anisotropic minerals under strain in the mantle (Karato, 1998a; Montagner, 1998). When detected, anisotropy can be an indicator of mantle strain and flow and improve our understanding of the dynamics of the mantle. Evidence for radial anisotropy was first inferred from the discrepancy between Rayleigh and Love waves by Anderson (1961), Aki and Kaminuma (1963) and McEvilly (1964). These observations prompted the inclusion of radial anisotropy in the upper 220 km, also referred to as the anisotropic zone, of the global reference Earth model PREM (Dziewonski and Anderson, 1981). It is now commonly accepted that the Earth is radially anisotropic at shallow depths (up to ~200 km). There is, however, no consensus on whether radial anisotropy is present beyond the anisotropic zone. While earlier studies of radial anisotropy used fundamental mode surface waves (Tanimoto and Anderson, 1984; Nataf et al., 1984; Montagner and Tanimoto, 1991; Ekström and Dziewonski, 1998; Shapiro and Ritzwoller, 2002), in recent years higher mode surface waves have been added to studies of radial anisotropy (Debayle and Kennett,

2000; Gung et al., 2003; Beghein et al., 2006; Maggi et al., 2006; Panning and Romanowicz, 2006; Sebai et al., 2006; Marone et al., 2007) with a potential to yield constraints on deeper mantle dynamics, down to the transition zone and lower mantle. Radially anisotropic shear wave velocity models tend to agree at long wavelengths only (Panning and Romanowicz, 2006), suggesting large uncertainties in these models. These uncertainties depend on the regularisation, parameterization, inverse method, data uncertainties etc. Model space search methods provide a way to obtain a full probability density function for the parameters through the mapping of the entire model space rather than just one preferred central value.

A previous (linearized) Monte Carlo model space search for radial anisotropy in seismic reference models of the mantle (Beghein et al., 2006) found no significant spherically averaged radial anisotropy beyond the anisotropic zone, while spherically averaged radial anisotropy was found up to 1000 km in an earlier study by Montagner and Kennett (1996). Panning and Romanowicz (2006) inverted for a three-dimensional radial anisotropic model and found faster vertically polarized shear wave speed associated with subducted slab material in the transition zone. There is a large consensus between the one-dimensional and three-dimensional radially anisotropic studies that the lower mantle is isotropic, except in D'' (Kendall and Silver, 1996; Karato, 1998b; Panning and Romanowicz, 2004). An isotropic lower mantle can be explained in terms of superplastic flow (Karato, 1998a), which does not result in any preferred orientation of minerals, even though, the minerals themselves are still highly anisotropic.

* Corresponding author. Tel.: +31 30 2535086; fax: +31 30 2533486.

E-mail address: kviss@geo.uu.nl (K. Visser).

In this paper, we inverted the fundamental and higher mode, azimuthally averaged, phase velocity maps of Visser et al. (2008) for a global radially anisotropic shear wave velocity model using a fully non-linear model space search approach. We use Rayleigh wave phase velocity maps for the fundamental and up to the sixth higher mode and Love wave phase velocity maps for the fundamental and up to the fifth higher mode. This provides us with a large dataset of higher modes, especially in comparison with previous radially anisotropic studies (Debayle and Kennett, 2000; Maggi et al., 2006), where the number of higher mode measurements are often few and up to a relatively low higher mode (second to fourth higher mode). Panning and Romanowicz (2006) and Marone et al. (2007) used a waveform inversion technique, therefore including all excited higher modes which extended the resolution of the anisotropic models into the lower mantle, especially in Panning and Romanowicz (2006) where the inclusion of body waveform data extended the resolution down to the core mantle boundary.

The use of a model space search approach in the inversion for shear wave velocities should provide us with realistic uncertainties. The phase velocity measurements were obtained using a model space search approach, yielding consistent uncertainties between all the measurements. These uncertainties have been propagated in the construction of the phase velocity maps (Visser et al., 2008) and used as prior information here. The combination of a model space search and the large number of higher mode measurements should provide us with a global radially anisotropic model with an improved depth resolution and consistent uncertainties which in turn should give us insight into the mantle dynamics at larger depths in the mantle. The modes we use should give a good resolution down to about 1500 km. We convert the relative phase velocity maps of Visser et al. (2008) into absolute phase velocities by adding PREM (Dziewonski and Anderson, 1981) and invert Rayleigh and Love wave dispersion curves separately, in a fully nonlinear approach, to obtain a global horizontally and vertically polarized shear wave velocity model. These models are then combined into a global radially anisotropic shear wave velocity model. While other studies (Ekström and Dziewonski, 1998; Debayle and Kennett, 2000; Maggi et al., 2006) have also used two separate inversions for the Rayleigh and Love wave data, they used a linearized approach using Fréchet derivatives. Ekström and Dziewonski (1998, supplement) showed that no significant bias was introduced by the use of isotropic fundamental mode sensitivity kernels and two separate inversions for V_{SH} and V_{SV} . We will need to verify whether in our case we are allowed to invert Rayleigh and Love wave dispersion curves separately.

2. Depth inversion

This study presents the last stage of a three three-stage inversion as proposed by Kennett and Yoshizawa (2002). A traditional two-stage approach of multimode waveform tomography consists of obtaining one-dimensional velocity perturbations through waveform fitting and inverting them, using the path average assumption, for a three-dimensional velocity model. The three-stage approach consists of obtaining one-dimensional dispersion models through waveform fitting in the first stage, building multimode phase velocity models as a function of frequency using the path average assumption in the second stage and an inversion for local wave speed properties to obtain the three-dimensional velocity model in the third stage. The one-dimensional dispersion model in the first stage is regarded as a representation of the character of multimode dispersion along the source–receiver path. This is not as limiting an assumption as the path average assumption in the two two-stage approach. Yoshizawa and Kennett (2002) showed that multiple one-dimensional shear wave velocity models obtained through waveform fitting with a slight difference in misfit share the same dispersion characteristics indicating that the one-dimensional velocity model in the first stage may be

regarded as a representation of the multimode dispersion characteristics along the source–receiver path.

In the first stage, we applied waveform fitting using a model space search approach (using the Neighbourhood Algorithm; Sambridge, 1999a,b) to obtain the fundamental and higher mode Love and Rayleigh wave phase velocity measurements (Visser et al., 2007). In the second stage (Visser et al., 2008), we inverted the fundamental and higher mode Love and Rayleigh wave phase velocity measurements for global isotropic and azimuthally anisotropic phase velocity models. The isotropic parts of the phase velocity models are now used in the third stage to obtain a radially anisotropic shear wave velocity model using a fully non-linear inversion of absolute dispersion curves. Montagner and Nataf (1986) showed that radial anisotropy is dependent on the Love parameters (A, C, L, N, F) (Love, 1927) which describe a transversely isotropic medium, while azimuthal anisotropy is dependent on the other elastic parameters (B, H, E, G). By using the isotropic phase velocity models of the second stage (Visser et al., 2008), we only have to worry about the five Love parameters. We perform a point-by-point depth inversion using a model space search approach. To keep the number of parameters low in this Monte Carlo search and inspired by previous work, we invert the Love and Rayleigh wave phase velocity models separately. Ekström and Dziewonski (1998, supplement) validated this approach for a linearized inversion using fundamental mode data. In the case of a fully non-linear approach, however, the validity of this approximation has not been shown. Therefore we first performed a test where we calculated fundamental and higher mode Love and Rayleigh wave dispersion curves for the anisotropic PREM model. We then separated the anisotropic PREM model in a horizontally polarized model (V_{PH} , V_{SH}) and a vertically polarized model (V_{PV} , V_{SV}) and calculated the Love and Rayleigh wave phase velocities separately assuming isotropy. We found that the resulting phase velocity differences are within the uncertainties of the phase velocity models of Visser et al. (2008) for all modes considered. Since anisotropic PREM contains only shallow anisotropy, we performed the same test for the results of our depth inversion at a few locations on the Earth. The differences in the phase velocities calculated assuming isotropy or anisotropy are again within the uncertainties of the phase velocity models (Fig. 1), indicating no significant difference between the two approaches. This test indicates that for our anisotropic model at least, we can invert Love and Rayleigh waves separately resulting in a considerable gain in CPU time (days rather than weeks).

We selected 492 locations, covering the Earth's surface according to a 6-fold triangular tessellation (equal area representation, Wang and Dahlen, 1995). At each point, we calculated the absolute local phase velocities from the selected fundamental and higher mode isotropic Love and Rayleigh wave phase velocity maps. The sampling of the Earth's surface is comparable to that of a spherical harmonic expansion of degree and order 20 (Wang and Dahlen, 1995), which is at the lower end of the resolution of the phase velocity maps of Visser et al. (2008). The fundamental mode phase velocity maps of Visser et al. (2008) have a resolution corresponding to spherical harmonic degree 25, the higher mode phase velocity maps have decreasing resolution (down to spherical harmonic degree 20, except for the phase velocity maps of the fifth higher mode Love which have a resolution corresponding to spherical harmonic degree 18). The change in resolution with the number of higher modes should therefore not affect our inferences. The phase velocity measurements used for the building of the phase velocity maps were obtained using a model space search approach. This provided us with consistent uncertainties on the measurements as well as on the phase velocity maps as described in Visser et al. (2008). At each location, we invert the local phase velocities of different modes, with the corresponding uncertainties. This will provide us with consistent posterior uncertainties given these prior uncertainties. The objective of the model space search is to find, for each location, the V_{SH} and V_{SV} model and

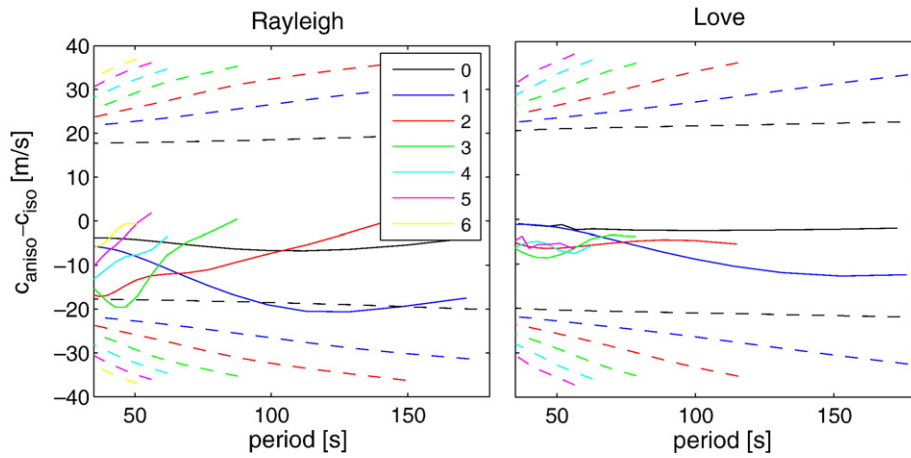


Fig. 1. The difference between the Love and Rayleigh fundamental (0) and higher mode (1–6) phase velocities calculated assuming anisotropic and isotropic profiles for a location in the Baltic Shield (58°N, 17°E). The dashed lines indicate the uncertainties for the phase velocity models of Visser et al. (2008). For Love, the isotropic model has V_S and V_P equal to V_{SH} and V_{PH} of the anisotropic model, for Rayleigh the isotropic model has V_S and V_P equal to V_{SV} and V_{PV} of the anisotropic model.

the Moho depth that fits the observed phase velocities for Love and Rayleigh waves, respectively.

2.1. Parameterization

We parameterize the shear wave velocity model using the same 12 natural cubic spline basis functions which have been used in the measurement stage (Fig. 2). The position and number of the spline basis functions were obtained after several tests with different parameterizations. A Backus–Gilbert resolution analysis showed that the twelve spline parameterization is optimal for the modes used here. The splines are more densely spaced in the upper mantle compared to the lower mantle to match the depth resolution of surface waves. As in Visser et al. (2008), we scaled the compressional wave velocity and density to the shear wave velocity model. For the compressional wave velocity, we chose the scaling relation of Ritsema and Van Heijst (2002) and for the density the scaling relation of Deschamps et al. (2001). Scaling relations are often used in depth inversions (see for example, Ekström and Dziewonski, 1998; Shapiro and Ritzwoller, 2002; Gung et al., 2003; Panning and Romanowicz, 2006) to reduce the number of parameters in the inverse problem to the best resolved parameters (V_{SH} , V_{SV}). Multiple studies (Ekström and Dziewonski, 1998; Gung et al., 2003) have shown that specific scaling relations did not affect the resulting velocity models much.

Crustal corrections are very important in surface wave tomography (Montagner and Jorbert, 1988; Mooney et al., 1998; Zhou et al., 2006; Marone et al., 2007; Bozdog and Trampert, 2008). Bozdog and

Trampert (2008) showed that accurate crustal corrections are more difficult for Love waves, due to the higher sensitivity to crustal structure. Radially anisotropic shear wave velocity models (combinations of Rayleigh (V_{SV}) and Love (V_{SH}) data) are, therefore, most affected by improper crustal corrections. We therefore follow Li and Romanowicz (1996) and add Moho depth as one additional parameter to the inversion. We do not perform corrections for any other crustal parameters but add an initial crustal model. Meier et al. (2007) obtained a crustal model by inverting fundamental mode phase velocities using a neural network approach. This crustal model consists of an average shear wave velocity for the crust and a Moho depth. For the frequencies we use, Moho depth is the important parameter and crustal velocities matter little (Meier et al., 2007). We therefore keep the crustal velocities fixed and vary Moho depth only. The first spline coefficient is therefore fixed. The second spline is defined at the specific Moho depth for the tessellation location. So, our final velocity parameterization consists of eleven splines from the Moho down to 1500 km and one extra parameter which is Moho depth. Both the V_{SH} as well as the V_{SV} inversion should provide similar Moho depths. Fig. 3 shows that this is indeed the case for the V_{SV} and V_{SH} models. The Moho depths resulting from both inversions are consistent. The best fitting line through the points is for $\text{Moho}_{SV} = \text{Moho}_{SH} + 0.5$ km and the standard deviation is 0.4 km. This range is well within the mean standard deviations of the Moho depths (3.0 km) from Meier et al. (2007), indicating that the differences between the Moho depths are not significant and the separate V_{SH} and V_{SV} inversions are consistent with each other.

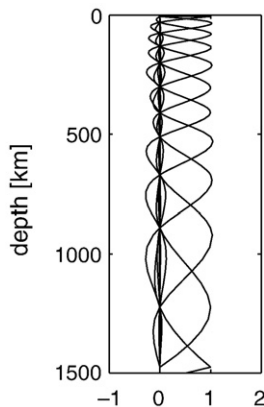


Fig. 2. Twelve natural cubic spline basis functions. The splines are numbered one to twelve from the top to the bottom (1500 km).

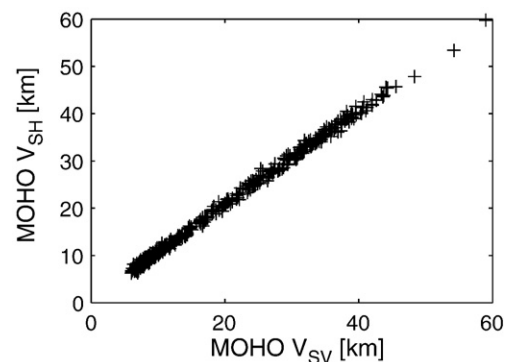


Fig. 3. Moho depths resulting from the inversion for V_{SV} (Rayleigh wave data) and the inversion for V_{SH} (Love wave data) for the 492 tessellation points.

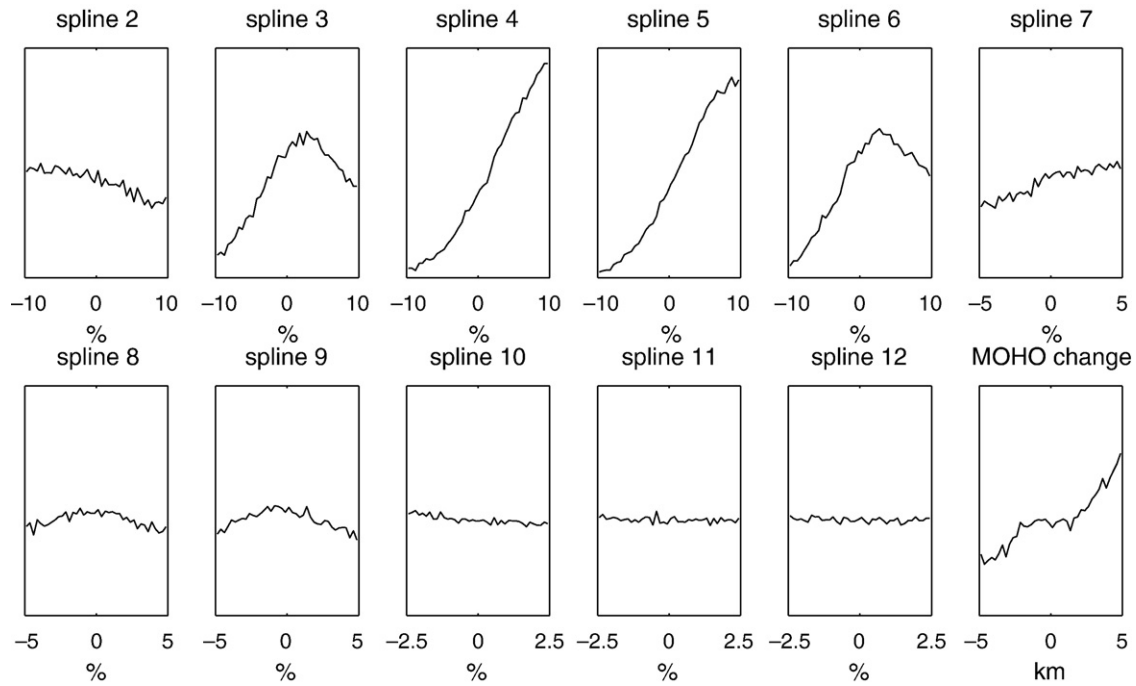


Fig. 4. One-dimensional marginals indicating the change in V_{SSH} inversion parameters (Fig. 2) from the reference model at the Baltic Shield (58°N, 17°E) location. The limits on the x-axis give the limit of the prior marginal.

For each tessellation point, we construct a shear wave velocity model, searching in a certain range around PREM (Dziewonski and Anderson, 1981), from the Moho down to 1500 km and adapt the Moho depth, searching around the model of Meier et al. (2007). The topography and the bathymetry, for the tessellation location, are fixed and taken from CRUST2.0 (Bassin et al., 2000). Below 1500 km, we assume PREM. For each model constructed this way, we calculate the

phase velocities using a normal mode code and compare them to the observations.

2.2. Model space search

For the model space search we use the Neighbourhood Algorithm (Sambridge, 1999a,b). The first part of the NA is a Monte Carlo search

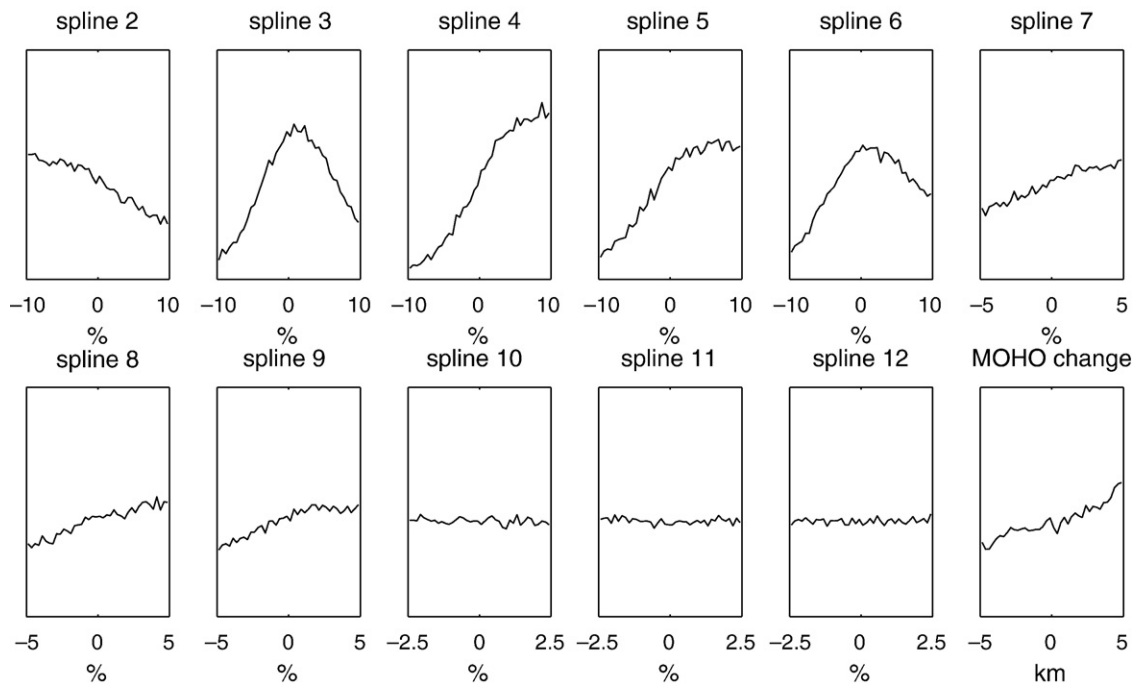


Fig. 5. One-dimensional marginals indicating the change in V_{SV} inversion parameters (Fig. 2) from the reference model at the Baltic Shield (58°N, 17°E) location. The limits on the x-axis give the limit of the prior marginal.

that uses the misfit to guide the model space search to areas of better fit. The χ^2 misfit between the observed absolute phase velocities and the calculated phase velocities for each velocity model is defined as

$$\chi^2 = \frac{1}{N} \sum_{i=1}^N \frac{(c_{\text{obs},i}^{\text{L,R}} - c_i^{\text{L,R}})^2}{(\sigma_{\text{obs},i}^{\text{L,R}})^2}, \quad (1)$$

where $c_{\text{obs}}^{\text{L,R}}$ are the observed phase velocities for Love (L) and Rayleigh (R) respectively and $\sigma_{\text{obs}}^{\text{L,R}}$ are the model uncertainties for the phase velocity maps (Visser et al., 2008). $c_i^{\text{L,R}}$ are the calculated phase velocities.

The nature of the model space search is determined by a few tuning parameters: the number of initial models (n_i), the number of iterations (n_{iter}), the number of new models sampled at each iteration (n_s) and the number of best misfit models at each iteration (n_r). At each iteration, the existing models are ranked according to their fit. In the Voronoi cells (nearest neighbourhood cells) of the n_r best fit models, n_s new models are randomly chosen after which all the models are ranked again according to their fit. The tuning parameters (n_r and n_s) determine how the model space is sampled. A large number for n_s and a small number for n_r lead to a very focused search, where the disadvantage is that some areas of good fit may be missed by this search. A large number for n_r (for example, equal to n_s) lead to a much broader (but also slower) search. For each point in the model space, a velocity model is constructed using the coefficients for the shear wave velocity splines, the change in Moho depth and the scaling relations between the shear wave velocity and the compressional wave velocity and density. For this velocity model, we compute the exact local eigenfunctions for the specific surface wave modes in our data and obtain the phase velocities for these modes. The problem is highly non-linear and, therefore, we need a very broad search ($n_i=100$, $n_{\text{iter}}=500$, $n_s=100$ and $n_r=100$) so as not to miss any well fitting areas. The total number of sampled models is 50,100 per inversion.

The model space is searched around a reference model. The reference model is PREM with the crust of the specific latitude–longitude location taken from Meier et al. (2007) and the topography and bathymetry information taken from CRUST2.0 (Bassin et al., 2000). In the upper mantle we allow a change of $\pm 10\%$, in the transition zone a change of $\pm 5\%$ and in the lower mantle a change of $\pm 2.5\%$ with respect to the reference model. We, further, allow the Moho depth to vary by ± 5.0 km. The decrease in the model space size with depth is motivated by results from previous shear wave velocity modelling (Su and Dziewonski, 1997; Ritsema et al., 1999; Panning and Romanowicz, 2006). The reference model only serves to define the search bounds and its choice is not as crucial as in a linearized inversion where Fréchet derivatives are calculated in the reference model. This first part of the Neighbourhood Algorithm produces an ensemble of velocity models with their corresponding fit (Eq. (1)) to the observed phase velocities.

2.3. Bayesian information

The second part of the NA (Sambridge, 1999b) extracts information from the whole ensemble of models. It computes the conditional posterior probability density function ($P(\mathbf{m}|\mathbf{d})$) of the model (\mathbf{m}) given the data (\mathbf{d}) as

$$P(\mathbf{m}|\mathbf{d}) = \kappa \rho(\mathbf{m})L(\mathbf{m}|\mathbf{d}), \quad (2)$$

where $\rho(\mathbf{m})$ is the prior probability distribution which depends on the parameterization, the search boundaries and the forward theory, κ is a normalization constant and $L(\mathbf{m}|\mathbf{d})$ is a likelihood function representing the fit to the observations defined as $L(\mathbf{m}|\mathbf{d}) = \exp(-1/2\chi^2)$. The NA first constructs an approximate posterior probability density (PPD) for the ensemble of models by assuming constant known PPD values in the Voronoi cells and then performs a couple of random walks using a

Gibbs sampler (Geman and Geman, 1984; Rothmann, 1986). After multiple random walks, the distribution will asymptotically resemble the approximate posterior probability density function. This resampled ensemble can be used in a Bayesian framework to infer information from the ensemble such as one- or two-dimensional marginals and the covariance matrix. The one-dimensional marginals of the separate V_{SH} and V_{SV} inversions can be jointly resampled to obtain one-dimensional marginals of anisotropic and isotropic anomalies. We define the Voight average isotropic shear wave velocity (Babuska and Cara, 1991) as

$$V_S^2 = \frac{2V_{\text{SV}}^2 + V_{\text{SH}}^2}{3}, \quad (3)$$

and the shear wave anisotropy as

$$\xi = \frac{V_{\text{SH}}^2}{V_{\text{SV}}^2}. \quad (4)$$

3. A detailed example

We illustrate our approach with an example for a location on the Baltic Shield (58°N, 17°E). We perform the Rayleigh and Love wave inversions and obtain one- and two-dimensional marginals that provide the full information on the entire ensemble of shear wave velocity models. Figs. 4 and 5 show the one-dimensional marginals for the V_{SH} and V_{SV} inversions, respectively. The one-dimensional marginals show how well we are able to resolve the individual spline coefficients (Fig. 2). Spline coefficients three to six are relatively well resolved, there are clearly defined areas of higher probability, while spline coefficients ten to twelve are completely unresolved (flat). From this we can infer that at this location, we are able to resolve V_{SH} and V_{SV} best from 75 km to 400 km, but we are unable to resolve shear wave velocity from 800 km to 1500 km. Comparing the one-dimensional marginals for the V_{SH} and V_{SV} inversions, we notice that the areas of highest probability are quite similar for both inversion indicating modest anisotropy. The two-dimensional marginals (Fig. 6) are important to identify trade-offs which show as diagonal alignments. Trade-offs exist, but they are weak compared to our inability to resolve shear wave speed at certain depths. The Moho in Figs. 4–6 is not well constrained. The average standard deviation for the Moho depth found by Meier et al. (2007) is ± 3.0 km. The allowed change in Moho depth we have chosen is ± 5.0 km, therefore we would not expect to find a well resolved Moho depth in this range. Fig. 6 shows that although the Moho depth is not well resolved, there is no trade-off with the second spline which is where a possible trade-off is expected to be highest. In general, the one-dimensional marginals (Figs. 4 and 5) are not Gaussian, and not even symmetric which reflects the non-linearity of the problem. This means that we cannot represent them by a simple mean and a standard deviation.

We jointly resample the one-dimensional marginals for V_{SH} and V_{SV} to obtain the one-dimensional marginals for the isotropic shear wave velocity and radial anisotropy (Eqs. (3) and (4)). Fig. 7 shows the one-dimensional marginals for anisotropy at the example location. Comparing the prior marginals (limits of the x -axis) with the posterior marginals, we have now obtained information on all spline coefficients (all marginals of the spline coefficients show a clearly defined maximum). This may seem surprising since the separate marginals for V_{SH} and V_{SV} show no information gain (flat marginals) for spline coefficients ten to twelve. The theorem for the association of probability density functions (see statistical textbooks) explains this. A particular case of association is the sum which is governed by the Central Limit Theorem. Here, the formation of ξ is more complicated and non-linear. Nevertheless, general properties remain the same: the result is a peaked probability density and its moments depend strongly on the individual spreads. It is difficult to have an intuition for the results, but for an unresolved spline for V_{SH}

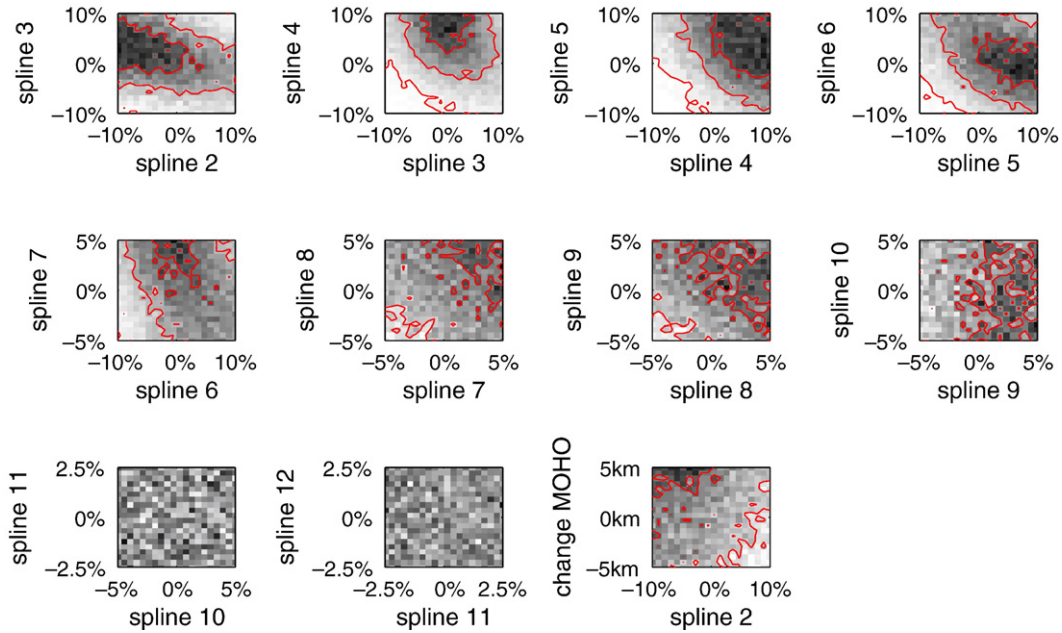


Fig. 6. Two-dimensional marginals for the inversion for V_{SV} at the Baltic Shield ($58^{\circ}N$, $17^{\circ}E$) location. The contour lines indicate 1σ , 2σ and 3σ . Darker shading means higher probability. The limits on the axis give the limit of the prior marginal. The reference is the reference model for the specific point.

and V_{SV} (e.g. #9) the standard deviation for ξ in percent is more than twice the initial sampling interval. For a resolved spline (e.g. #3) the standard deviation for ξ in percent is the same as the initial sampling interval. The standard deviations are not too meaningful, since most marginals are skewed, except for the ones corresponding to unresolved parameters. Still this gives a feeling of what to expect.

4. Spherically averaged anisotropy

We performed the depth inversion and obtained the one-dimensional marginals for anisotropy for all tessellation locations.

The one-dimensional marginals at each location are now averaged to compute the spherically averaged anisotropy at each depth. We performed the sum by resampling the individual marginals. The result is governed by the Central Limit Theorem and therefore the average probability density at each depth is nearly Gaussian. It is thus meaningful to represent its mean and standard deviation. Fig. 8 shows the spherically averaged anisotropy. In the anisotropic zone, the positive ($V_{SH} > V_{SV}$) spherically averaged anisotropy corresponds quite well to anisotropic PREM as well as the results obtained by previous studies (Montagner and Kennett, 1996; Beghein et al., 2006; Zhou et al., 2006) of spherically averaged anisotropy. At 220 km, we observe

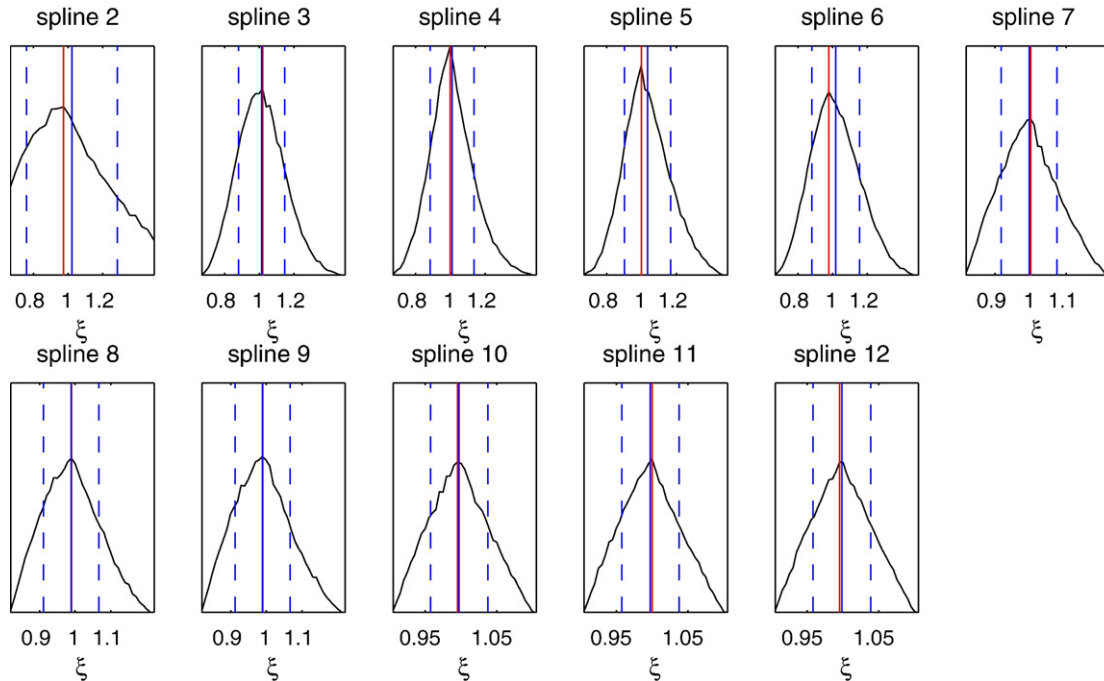


Fig. 7. One-dimensional posterior marginals for the anisotropic parameters at the Baltic Shield ($58^{\circ}N$, $17^{\circ}E$) location. The red line indicates the maximum value, the blue line indicates the mean and the dashed blue lines the mean \pm one standard deviation. The limits on the x-axis give the limit of the prior marginal.

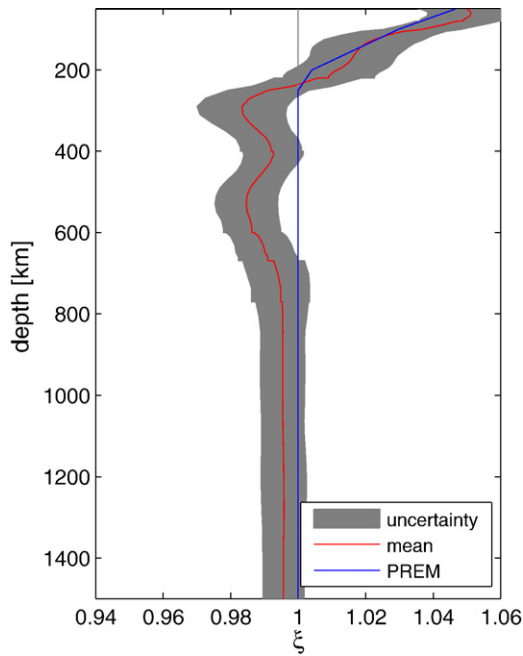


Fig. 8. Spherically averaged anisotropy. Also indicated are the 95% confidence levels (two standard deviations) and the anisotropic PREM model (Dziewonski and Anderson, 1981).

a sign change in the average anisotropy from positive ($V_{SH} > V_{SV}$) to negative ($V_{SV} > V_{SH}$) anisotropy, which was also observed by Montagner and Kennett (1996), Beghein et al. (2006), Zhou et al. (2006), although Beghein et al. (2006) concluded that it is not significant due to the large uncertainties in their linearized inversion. We find significant (95% confidence or larger than two standard deviations) negative average anisotropy from 220 km down to the transition zone. The change in the sign of anisotropy could indicate a change from predominantly horizontal flow in the lithosphere and asthenosphere to predominantly vertical flow in the deeper mantle assuming that anisotropy is caused by the lattice preferred orientation of intrinsically anisotropic mantle minerals by finite strain due to mantle flow. Although the presence of water could significantly complicate this simple view (Jung and Karato, 2001). The peak in negative anisotropy around 300 km was also observed by Zhou et al. (2006), although this study only used fundamental mode data and the resolution should therefore not extend much beyond a depth of 400 km. The significant negative anisotropy continues through the transition zone which disagrees with Montagner and Kennett (1996) who found positive anisotropy in the transition zone. In the lower mantle (down to 1500 km), we find no significant average anisotropy in agreement with previous studies.

5. How probable is laterally varying anisotropy?

Our individual posterior probability density functions for ξ are clearly skewed (Fig. 7), which makes it difficult to represent them by a

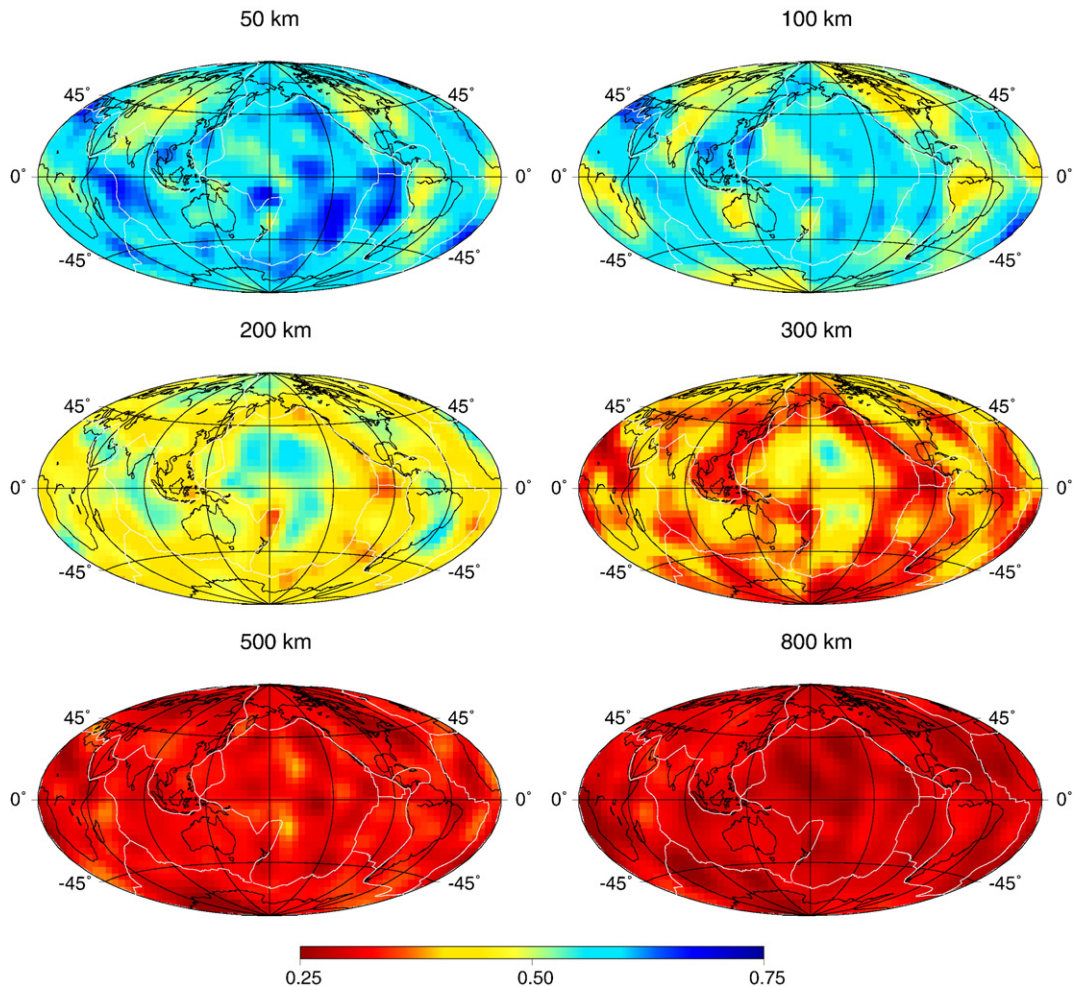


Fig. 9. Maps of probability of anisotropy ($V_{SH} > V_{SV}$).

mean and a standard deviation. But our posterior probability density functions allow us to calculate the probability that V_{SH} is larger than V_{SV} , for instance, which is the area under the curve of the one-dimensional marginal for which ξ is larger than one. Fig. 9 shows the distribution of the total probability of positive ($V_{SH} > V_{SV}$) anisotropy for various depths. Since the total area under a probability density function is one ($P(\xi > 1) + P(\xi < 1) = 1$), the low probabilities of positive anisotropy (Fig. 9) show the high probabilities of negative ($V_{SH} < V_{SV}$) anisotropy. In the anisotropic zone, we find a high probability of positive ($V_{SH} > V_{SV}$) anisotropy, except for the cratonic areas. At 300 km, we see a change to a high probability for negative anisotropy associated mainly with subduction zones and mid-ocean ridges. Gung et al. (2003) and Panning and Romanowicz (2006) found evidence for $V_{SH} > V_{SV}$ beneath cratons between 200 and 350 km. We also find, in the same depth region, a slightly higher probability for $V_{SH} > V_{SV}$ beneath cratons compared to other regions. Below the transition zone, we find a high probability of negative anisotropy, but this does not give any details about the amplitude of anisotropy. Just as easily, our marginals allow us to compute the probability that anisotropy is larger than 1% ($P(|\xi| > 1.01)$) or larger than 2% ($P(|\xi| > 1.02)$). Figs. 10 and 11 show the probability of anisotropy with an amplitude larger than 1% and 2%, respectively for different tectonic regions (defined from 3SMAC, Nataf and Richard, 1996). We computed the average probabilities over these regions by resampling the one-dimensional marginals.

From this averaged one-dimensional marginal for the region, we computed the probability of anisotropy with an amplitude larger than 1% and 2%. Overall, we find the same pattern as for the average anisotropy; a high probability of positive anisotropy in the anisotropic zone, and a high probability of negative anisotropy down through the

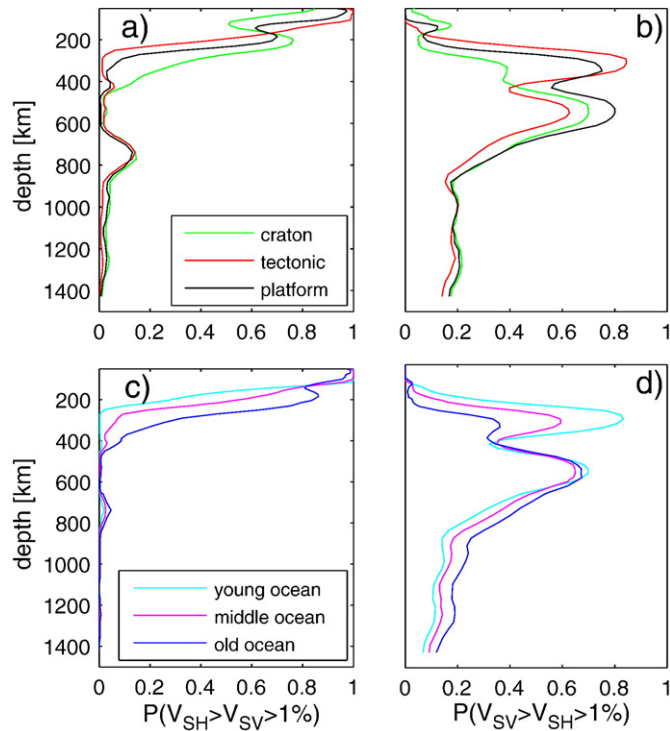


Fig. 10. The probability that the amplitude of anisotropy is larger than 1% for different tectonic areas. The definition of the tectonic areas is taken from 3SMAC (Nataf and Richard, 1996). Young oceans correspond to oceanic crust younger than 50 Ma, middle oceans correspond to oceanic crust between 50 Ma and 100 Ma and old oceans correspond to oceanic crust older than 100 Ma. The probability of a higher than 1% positive anisotropy for cratonic, tectonic and platform areas (a), young, middle and old oceans (b) and the probability of a higher than 1% negative anisotropy for cratonic, tectonic and platform areas (c), young, middle and old oceans (d).

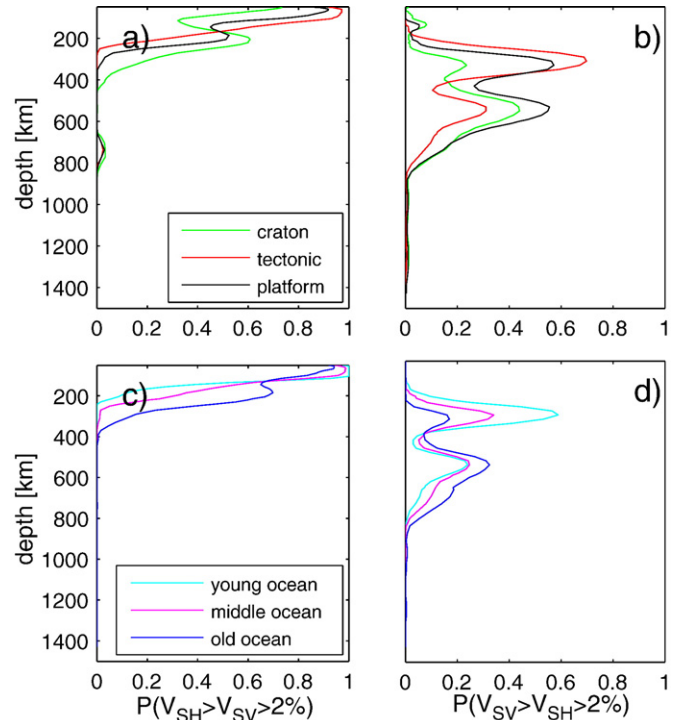


Fig. 11. The probability that the amplitude of anisotropy is larger than 2% for different tectonic areas. The definition of the tectonic areas is taken from 3SMAC (Nataf and Richard, 1996). Young oceans correspond to oceanic crust younger than 50 Ma, middle oceans correspond to oceanic crust between 50 Ma and 100 Ma and old oceans correspond to oceanic crust older than 100 Ma. The probability of a higher than 2% positive anisotropy for cratonic, tectonic and platform areas (a), young, middle and old oceans (b) and the probability of a higher than 2% negative anisotropy for cratonic, tectonic and platform areas (c), young, middle and old oceans (d).

transition zone with two peaks around 300 km and 550 km. The probability of a high amplitude ($>2\%$) positive anisotropy in the anisotropic zone is high (>0.95) (Fig. 11). The anisotropy in the transition zone is likely smaller in amplitude since only the probability of negative anisotropy with an amplitude larger than 1% is as high as 0.6–0.8. In the lower mantle, the probability that the amplitude of anisotropy is larger than 1% is exceedingly low. If present, the amplitude of anisotropy in the lower mantle is too small to be mapped with any confidence.

6. Discussion

In the uppermost mantle we find a high probability of anisotropy with fast horizontally polarized shear waves in the oceans and continents (Fig. 9). The amplitude of the anisotropy is likely to be large ($>2\%$, Fig. 11). The probability of a large amplitude of anisotropy shows a difference between different regions. In the first 200 km, the oceanic areas show the highest probabilities of positive ($V_{SH} > V_{SV}$) anisotropy, while from 200 to 400 km the positive anisotropy is mainly found in the cratonic areas and old oceans (Figs. 10a and 11a). This corresponds roughly to an earlier observation by Gung et al. (2003), who found fast horizontally polarized shear wave anisotropy underneath oceans from 80 to 250 km and underneath cratons from 250 to 400 km. They explained this by a low-viscosity asthenospheric channel at different depths underneath oceans and continents.

From 200 km to 400 km we find prominent features of fast vertically polarized shear wave anisotropy at mid-ocean ridges and subduction zones (Fig. 9). The tectonic regions (Figs. 10 and 11) and young oceanic regions show indeed much higher probability of negative ($V_{SV} > V_{SH}$) anisotropy from 200 to 400 km. The probability of a significant amplitude (1%/2%) of negative ($V_{SV} > V_{SH}$) anisotropy (Figs. 10 and 11) shows a peak at

300 km, for all tectonic areas. The probability that the amplitude of negative anisotropy is more than 1% is more than 0.8 for the young oceans and tectonic areas. The probability that the amplitude is larger than 2% is 0.6 for the mid-ocean ridges and 0.7 for the tectonic areas, indicating a possible amplitude difference between the mid-ocean ridges and subduction zones. This agrees with the models of Gung et al. (2003), Panning and Romanowicz (2006), and Zhou et al. (2006) who also found negative anisotropy associated with mid-ocean ridges and subduction zones at these depths. Zhou et al. (2006) found negative anisotropy at mid-ocean ridges visible from 120 km down to the transition zone. Fig. 10d shows that the probability of negative anisotropy, with an amplitude larger than 1%, is different for young oceans and middle aged oceans from about 120 km down to the transition zone. This corresponds to the finding of Zhou et al. (2006).

If we assume that anisotropy is caused by the lattice preferred orientation of intrinsically anisotropic minerals under strain in the mantle, we observe evidence of predominantly horizontal flow in the anisotropic zone and predominantly vertical flow below. The horizontal flow in the lithosphere has probably been frozen in at the time of the formation of the lithosphere or at the last major episode of its deformation while the horizontal flow in the asthenosphere is probably due to plate motion. Down from about 120 km we observe evidence of vertical flow at mid-ocean ridges, and down from about 200 km we also observe evidence of vertical flow at subduction zones. The vertical flow associated with the mid-ocean ridges and subduction zones extends at least down to the transition zone.

In the transition zone we find in general a high probability of radial anisotropy with fast vertically polarized shear waves ($P < 0.40$, Fig. 9). Panning and Romanowicz (2006) found anisotropy with fast vertically polarized shear waves associated with subduction zones in the transition zone. The total probability of large ($>2\%$) anisotropy (Fig. 11b,d) shows a peak at 550 km, but is at most 0.5. The amplitude of anisotropy in the transition zone is likely between 1% and 2% (compare Figs. 10b,d and 11b,d). Also, the amplitude of negative anisotropy seems to be lower for the oceanic areas. The observed anisotropy in the transition zone could be explained by dominant vertical flow. However, Jung and Karato (2001) showed that the addition of water changes the lattice preferred orientation of olivine under high stresses. Under these conditions, the direction of the faster S-wave polarization is perpendicular to the flow direction as opposed to parallel in other conditions. If the transition zone has a high water content, our observations correspond to a partially inhibited flow across the 670 km discontinuity. The interpretation of the anisotropy in the transition zone and lower mantle in terms of mantle flow remains ambiguous due to the complicated relation between the anisotropic properties of the mantle minerals and the unknown presence of water.

Although Fig. 9 shows a large probability of fast vertically polarized shear wave anisotropy in the lower mantle, the probability of a significant amplitude ($>1\%$) is low (Fig. 10b,d). The lower mantle, at least down to 1500 km, is most likely isotropic, which corresponds to earlier findings of Panning and Romanowicz (2006) and Meade et al. (1995). An isotropic lower mantle could be explained by superplastic flow (Karato, 1998a), because in superplastic flow the minerals do not align in preferred orientations. Even though the minerals themselves are highly anisotropic, seismic waves would see an isotropic lower mantle.

7. Conclusions

We performed the last step in a three-stage inversion (Yoshizawa and Kennett, 2002) for radially anisotropic structure of the mantle. In the first stage, we applied waveform fitting using a model space search approach to obtain fundamental and higher mode Love and Rayleigh wave phase velocity measurements (Visser et al., 2007). The second stage (Visser et al., 2008) consisted of inverting the fundamental and higher mode Love and Rayleigh phase velocity measurements to obtain

global isotropic and azimuthally anisotropic phase velocity maps. In the third stage, presented here, we invert the isotropic phase velocity maps, including their uncertainties, for Love and Rayleigh waves separately to obtain a global V_{SH} and V_{SV} model. We invert the phase velocity maps using a fully non-linear model space search approach. We tested that we could invert Love and Rayleigh wave phase velocities separately. The model space search provides us with the whole ensemble of V_{SV} and V_{SH} models and we resample these ensembles to obtain an ensemble of isotropic and anisotropic models. Since we know not only the best anisotropic model but the whole ensemble of models we can compute the total probability of positive ($V_{SH} > V_{SV}$) or negative ($V_{SV} > V_{SH}$) anisotropy as well as compute the probability that the amplitude of anisotropy is above a certain amplitude (1%, 2%).

We find a high probability of anisotropy with fast horizontally propagating shear waves (horizontal flow), in the upper mantle down to 200 km. For cratons, this fast horizontally propagating shear wave anisotropy (horizontal flow) is found down to 400 km. The amplitude of positive anisotropy in the uppermost mantle is likely to be large ($>2\%$) in the lithosphere and decreases down to 200 km. In the lithosphere, the observed anisotropy could be related to anisotropy frozen in at the time of formation or last significant deformation. From about 120 km, we find a high likelihood of fast vertically polarized shear wave anisotropy (vertical flow) associated with mid-ocean ridges and from about 200 km the fast vertically polarized shear wave anisotropy is also associated with subduction zones. This extends down to the transition zone. The amplitude of this anisotropy just above the transition zone (300 km) is probably large ($>2\%$). The transition zone is dominated by fast vertically polarized shear wave anisotropy, although the amplitude is likely lower (between 1% and 2%). The lower mantle down to 1500 km appears isotropic.

Acknowledgements

We would like to thank Barbara Romanowicz and an anonymous reviewer for their constructive comments. We would like to thank M. Sambridge for providing the Neighbourhood Algorithm programs. The calculations for this study were performed on a 64-node cluster financed by the Dutch National Science foundation under grant NWO: VICI1865.03.007. Other computational resources for this work were provided by the Netherlands Research Center for Integrated Solid Earth Science (ISES 3.2.5 High End Scientific Computation Resources). Fig. 9 was generated using the Generic Mapping Tools (GMT; Wessel and Smith (1995)).

References

- Aki, K., Kaminuma, K., 1963. Love waves from the Aleutian shock of March 9, 1957. Bull. Earthq. Res. Inst. 41, 243–259.
- Anderson, D.L., 1961. Elastic wave propagation in layered anisotropic media. J. Geophys. Res. 66, 2953–2963.
- Babuska, V., Cara, M., 1991. Seismic Anisotropy in the Earth. Kluwer Academic Press, Boston, Massachusetts.
- Bassin, C., Laske, G., Masters, G., 2000. The current limits of resolution for surface wave tomography in North America. EOS Trans. AGU 81, F897.
- Beghein, C., Trampert, J., van Heijst, H.J., 2006. Radial anisotropy in seismic reference model of the mantle. J. Geophys. Res. 111, B02303. doi:10.1029/2005JB003728.
- Bozdag, E., Trampert, J., 2008. On crustal corrections in surface wave tomography. Geophys. J. Int. 172, 1066–1082.
- Debayle, E., Kennett, B.L.N., 2000. Anisotropy in the Australian upper mantle from Love and Rayleigh waveform inversion. Earth Planet. Sci. Lett. 184, 339–351.
- Deschamps, F., Snieder, R., Trampert, J., 2001. The relative density to shear velocity scaling in the uppermost mantle. Phys. Earth Planet. Inter. 124, 193–211.
- Dziewonski, A.M., Anderson, D.L., 1981. Preliminary Reference Earth model. Phys. Earth Planet. Inter. 25, 297–356.
- Ekström, G., Dziewonski, A.M., 1998. The unique anisotropy of the Pacific upper mantle. Nature 394, 168–172.
- Geman, A.E., Geman, D., 1984. Stochastic relaxation, gibbs distributions and the bayesian restoration of images. IEEE Trans. Pattern Anal. Mach. Intell. 6, 721–741.
- Gung, Y., Panning, M., Romanowicz, B., 2003. Global anisotropy and the thickness of continents. Nature 422, 707–711.
- Jung, H., Karato, S., 2001. Water-induced fabric transitions in olivine. Science 293, 1460–1463.

- Karato, S., 1998a. Seismic anisotropy in the deep mantle, boundary layers and the geometry of mantle convection. *Pure Appl. Geophys.* 151, 565–587.
- Karato, S.I., 1998b. Some remarks on the origin of seismic anisotropy in the D'' layer. *Earth Planets Space* 50, 1019–1028.
- Kendall, J.M., Silver, P.G., 1996. Constraints from seismic anisotropy on the nature of the lowermost mantle. *Nature* 381, 409–412.
- Kennett, B.L.N., Yoshizawa, K., 2002. A reappraisal of regional surface wave tomography. *Geophys. J. Int.* 150, 37–44.
- Li, X.D., Romanowicz, B., 1996. Global mantle shear wave velocity model developed using nonlinear asymptotic mode coupling theory. *J. Geophys. Res.* 101, 22,245–22,272.
- Love, A.E.H., 1927. *A Treatise on the Theory of Elasticity*. Cambridge University Press.
- Maggi, A., Debayle, E., Priestley, K., Barruol, G., 2006. Multimode surface waveform tomography of the Pacific Ocean: a closer look at the lithospheric cooling signature. *Geophys. J. Int.* 166, 1384–1397.
- Marone, F., Gung, Y., Romanowicz, B., 2007. Three-dimensional radial anisotropic structure of the North-American upper mantle from inversion of surface waveform data. *Geophys. J. Int.* 171, 206–222.
- McEvilly, T.V., 1964. Central US crust–upper mantle structure from Love and Rayleigh wave phase velocity inversion. *Bull. Seismol. Soc. Am.* 54, 1997–2015.
- Meade, C., Silver, P.G., Kaneshima, S., 1995. Laboratory and seismological observations of lower mantle isotropy. *Geophys. Res. Lett.* 22, 1293–1296.
- Meier, U., Curtis, A., Trampert, J., 2007. Fully nonlinear inversion of fundamental mode surface waves for a global crustal model. *Geophys. Res. Lett.* 34, L16304. doi:10.1029/2007/GL030989.
- Montagner, J.P., 1998. Where can seismic anisotropy be detected in the Earth's mantle? *Pure Appl. Geophys.* 151, 223–256.
- Montagner, J.P., Jorbert, N., 1988. Vectorial tomography – ii. Application to the Indian Ocean. *Geophys. J. Int.* 94, 309–344.
- Montagner, J.P., Kennett, B.L.N., 1996. How to reconcile body-wave and normal-mode reference earth models. *Geophys. J. Int.* 125, 229–248.
- Montagner, J.P., Nataf, H. C., 1986. A simple method for inverting the azimuthal anisotropy of surface waves. *J. Geophys. Res.* 91, 511–520.
- Montagner, J.P., Tanimoto, T., 1991. Global upper mantle tomography of seismic velocities and anisotropies. *J. Geophys. Res.* 96, 20337–20351.
- Mooney, W.D., Laske, G., Masters, G., 1998. CRUST 5.1: a global crustal model at 5 degrees by 5 degrees. *J. Geophys. Res.* 103, 727–748.
- Nataf, H.C., Richard, Y., 1996. 3SMAC: an a priori tomographic model of the upper mantle based on geophysical modeling. *Phys. Earth Planet. Inter.* 95, 101–122.
- Nataf, H.C., Nakanishi, I., Anderson, D.L., 1984. Anisotropy and shear velocity heterogeneity in the upper mantle. *Geophys. Res. Lett.* 11, 109–112.
- Panning, M.P., Romanowicz, B.A., 2004. Inferences on flow at the base of the Earth's mantle based on seismic anisotropy. *Science* 303, 351–353.
- Panning, M., Romanowicz, B., 2006. A three-dimensional radially anisotropic model of shear velocity in the whole mantle. *Geophys. J. Int.* 167, 361–379.
- Ritsema, J., Van Heijst, H., 2002. Constraints on the correlation of P- and S-wave velocity heterogeneity in the mantle from P,PP,PPP and PKPab traveltimes. *Geophys. J. Int.* 149, 482–489.
- Ritsema, J., van Heijst, H.J., Woodhouse, J.H., 1999. Complex shear wave velocity structure imaged beneath Africa and Iceland. *Science* 286, 1925–1928.
- Rothmann, D.H., 1986. Automatic estimation of large residual statics corrections. *Geophysics* 51, 332–346.
- Sambridge, M., 1999a. Geophysical inversion with a neighbourhood algorithm— I. Searching a parameter space. *Geophys. J. Int.* 138, 479–494.
- Sambridge, M., 1999b. Geophysical inversion with a neighbourhood algorithm— II. Appraising the ensemble. *Geophys. J. Int.* 138, 727–746.
- Sebai, A., Stutzmann, E., Montagner, J.P., Sicilia, D., Beucler, E., 2006. Anisotropic structure of the African upper mantle from Rayleigh and Love wave tomography. *Phys. Earth Planet.* 155, 48–62.
- Shapiro, N.M., Ritzwoller, M.H., 2002. Monte-Carlo inversion for a global shear-velocity model of the crust and upper mantle. *Geophys. J. Int.* 151, 88–105.
- Su, W., Dziewonski, A., 1997. Simultaneous inversion for 3-D variations in shear and bulk velocity in the mantle. *Phys. Earth Planet. Inter.* 100, 135–156.
- Tanimoto, T., Anderson, D.L., 1984. Mapping convection in the mantle. *Geophys. Res. Lett.* 11, 287–290.
- Visser, K., Lebedev, S., Trampert, J., Kennett, B.L.N., 2007. Global love wave overtone measurements. *Geophys. Res. Lett.* 34, L03302. doi:10.1029/2006GL028671.
- Visser, K., Trampert, J., Kennett, B.L.N., 2008. Global anisotropic phase velocity maps for higher mode Love and Rayleigh waves. *Geophys. J. Int.* 172, 1016–1032.
- Wang, Z., Dahlen, F.A., 1995. Spherical-spline parameterization of three-dimensional Earth models. *Geophys. Res. Lett.* 22, 3099–3102.
- Wessel, P., Smith, W.H.F., 1995. New version of the generic mapping tools released. *EOS Trans. AGU* 76, 329.
- Yoshizawa, K., Kennett, B.L.N., 2002. Non-linear waveform inversion for surface waves with a neighbourhood algorithm – application to multimode dispersion measurements. *Geophys. J. Int.* 149, 118–133.
- Zhou, Y., Nolet, G., Dahlen, F.A., Laske, G., 2006. Global upper-mantle structure from finite-frequency surface wave tomography. *J. Geophys. Res.* 111, B04304. doi:10.1029/2005JB003677.